Architecture Effects

DOI: 10.1002/ange.201105028

Facet-Mediated Photodegradation of Organic Dye over Hematite Architectures by Visible Light**

Xuemei Zhou, Jinyao Lan, Gang Liu,* Ke Deng, Yanlian Yang, Guangjun Nie, Jiaguo Yu,* and Linjie Zhi*

Structure–reactivity correlations are a central theme in heterogeneous catalysis.[1–4] In general, the crystallographic surface structure of a catalyst is determined by its exposed facets, and the enclosed facets of a particle-like catalyst in turn determine its geometric shape as well as catalytic properties. Tuning the shape of catalysts, therefore, is essential in developing new catalysts and modifying existing ones with desirable reactivity, selectivity, and stability. Indeed, great advances have been achieved on model catalysts, and insights into the structure–reactivity correlations are crucial not only for our understanding of catalytic processes, but also for generating new concepts to guide the rational design of practical catalysts.[5–8]

In recent years, significant attention has been directed towards using solar-driven photocatalysts to degrade aqueous organic pollutants (for example, azo dyes).[9–13] In view of being naturally abundant and environmentally benign, iron oxides show great promise. Among iron oxides, hematite (α-Fe_2O_3) is the most thermodynamically stable semiconductor ($E_g = 2.1$–2.2 eV) that can absorb visible light, that is, a substantial fraction of the solar spectrum. α-Fe_2O_3 has a wide range of applications, such as light-induced water splitting,[14] solar cells,[15] lithium ion batteries,[16] and biotechnology.[17] Most studies to date have been carried out on powder substrates in which particle shapes are inherently not well-defined, making it difficult to explore the structure–reactivity correlations. While the vast majority of studies on the impact of particle shape on photocatalytic reactivity are limited to titanium dioxide (TiO_2),[18–27] far less information is available regarding the shape effects on other photocatalysts, including iron oxides. In this regard, systematic studies on heterogeneous photo-Fenton catalysis, a technologically promising process in wastewater treatment, by iron-bearing nanocatalysts with particular shapes are still lacking.[28,29] Over the past decade, size, shape, and architecture control of low-dimensional nanomaterials (for example, nanodots, nanorods, and nanosheets) with unusual properties has seen rapid growth.[30–36] For example, in one-dimensional (1D) anisotropic nanostructures, it is possible to enhance the photoreactivity by tuning the direction and path of photogenerated charge carriers through quantum confinement while minimizing the e^-–h^+ recombination.[37,38] Herein, we investigate visible-light-induced photodegradation of model dye rhodamine B (RhB) in the presence of hydrogen peroxide (H_2O_2) over hematite architectures, namely 1D nanorods, 2D nanoplates, and 3D nanocubes. Herein we use "architectures" to describe hematite nanostructures that can be assembled by nano-building units by oriented attachment.[35,36,39] To the best of our knowledge, this is the first study to investigate heterogeneous photo-Fenton catalysis by nanocatalysts with well-defined architectures.

The detailed synthesis of α-Fe_2O_3 architectures[39–42] is described in the Experimental Section and the Supporting Information. The structure, stoichiometry, and oxidation state of the as-prepared α-Fe_2O_3 architectures were characterized using X-ray diffraction (XRD; Supporting Information, Figure S1a), micro-Raman (Supporting Information, Figure S1b), and high-resolution X-ray photoelectron spectroscopy (XPS; Supporting Information, Figure S1c,d), and results demonstrate that all samples are pure α-Fe_2O_3 with a rhombohedral hexagonal phase (space group $R\bar{3}c$). The morphology and crystallinity of as-prepared α-Fe_2O_3 architectures were analyzed using transmission electron microscopy (TEM), high-resolution TEM (HRTEM), scanning electron microscopy (SEM), and atomic force microscopy (AFM). A TEM image for 2D nanoplates is shown in Figure 1a. All of the nanoplates display a well-defined hexagonal shape. Based on a SEM (Supporting Information, Figure S2a) and TEM analysis (Figure 1a; Supporting Information, Figure S2b), the width and thickness of the plates is determined to be (208.5 ± 27.3) and (14.6 ± 2.6) nm, respectively. A representative HRTEM image (Figure 1b) and fast Fourier transforms (FFT; inset in Figure 1b) show the lattice fringe to be 0.25 nm, which is consistent with (110), (−120), and (−210) planes, respectively. Thus, the resulting basal plane is (001). Vertically aligned plates that are frequently observed (Supporting Information, Figure S2b,c) are wedge-shaped and the lateral facets are ascribed to {102}.[42] A TEM

---

[*] X. M. Zhou, J. Y. Lan, Prof. G. Liu, Prof. K. Deng, Prof. Y. L. Yang, Prof. G. J. Nie, Prof. L. J. Zhi
National Center for Nanoscience and Technology
Beijing, 100190 (China)
E-mail: liug@nanoctr.cn
zhilj@nanoctr.cn
Prof. J. G. Yu
State Key Laboratory of Advanced Technology for Materials Synthesis and Processing, Wuhan University of Technology
Wuhan, 430070 (China)
E-mail: jiaguoyu@yahoo.com

[**] We thank Prof. Wayne Goodman from Texas A&M University for his valuable opinion on this manuscript. This work was supported by the National Basic Research Program of China (2007CB936802, 2010CB933600), the National Science Foundation of China (20933008, 20973044), MOST (2009AA03Z328, 2009DPA41220), and the Chinese Academy of Sciences (KJCX-2-YW-M11, KJCX-2-YW-H21).

Supporting information for this article is available on the WWW under http://dx.doi.org/10.1002/anie.201105028.

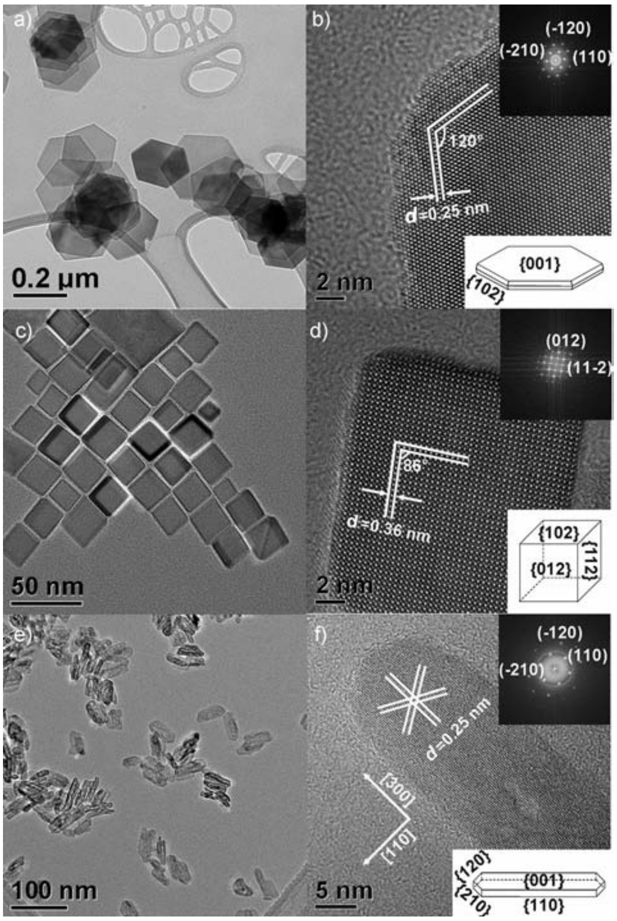

Figure 1. Representative morphologies and structures of α-Fe_2O_3 architectures. a) TEM image and b) HRTEM image of 2D α-Fe_2O_3 nanoplates. Insets: FFT pattern and drawing of a plate. c) TEM image and d) HRTEM image of 3D α-Fe_2O_3 nanocubes. Insets: FFT pattern and drawing of a cube. e) TEM image and f) HRTEM image of 1D α-Fe_2O_3 nanorods. Insets: FFT pattern and drawing of a rod.

image (Figure 1 c) shows that α-Fe_2O_3 3D nanocubes appear to be square in shape with an average size of (22.0 ± 3.2) nm. A HRTEM image (Figure 1 d) and corresponding FFT (inset in Figure 1 d) indicate that the lattice fringe is 0.36 nm. A close look at this cube reveals that the shape is pseudocubic and one of dihedral angles between adjacent lateral facets is 86°. The above data demonstrate that the cubes are enclosed by {012}, {102}, and {112} facets.[43] The TEM image in Figure 1 e reveals that the majority of 1D nanorods exhibit nearly faceted ends with a needle shape. Statistical analysis of dimensional distributions of rods based on TEM and AFM (Supporting Information, Figure S2d) indicates that the average length, width, and height is (40.3 ± 8.7), (10.9 ± 5.0), and (5.0 ± 1.2) nm, respectively. A HRTEM image (Figure 1 f) and FFT pattern (inset in Figure 1 f) indicate that three sets of lattice fringes (0.25 nm) fit well to the α-Fe_2O_3 (110), (−120), and (−210) planes, respectively. Therefore, the basal plane for α-Fe_2O_3 nanorods is (001). The physical parameters of the as-prepared samples, including dimensions, specific surface areas, and dominant facets are summarized in Table 1. On the basis of the above analysis, 1D nanorods, 2D nanoplates, and 3D nanocubes offer crystallographically distinct facets that are expected to be photocatalytically different.

The photocatalytic activity of the as-prepared samples was evaluated for RhB photodegradation under visible-light illumination. Experimental conditions were adapted from those of our previous work to be optimal for photocatalytic comparisons among iron oxide particles.[47] The temporal UV/Vis spectral changes of RhB aqueous solutions as a function of irradiation time are shown in the Supporting Information, Figure S3; with increasing irradiation time, the absorbance in both visible and UV regions decreased and the positions of major absorbance were shifted to low wavelength, in particular for samples with α-Fe_2O_3 nanocubes and nanorods. Figure 2 shows the changes of RhB relative concentrations as

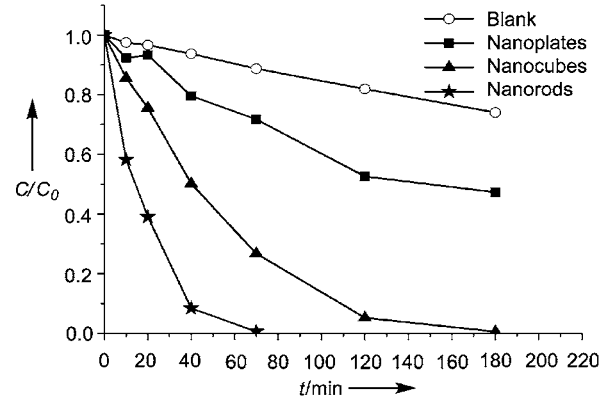

Figure 2. Photodegradation of RhB on α-Fe_2O_3 with different architectures under visible-light illumination in the presence of H_2O_2 additive. (Blank: photolysis in the presence of H_2O_2 only.) Reaction conditions: RhB concentration 2×10^{-5} M, catalyst concentration 0.2 $g L^{-1}$, H_2O_2 molar concentration 50 mM, initial pH 6.8, 300 W Xe-lamp ($\lambda > 420$ nm) with an average light intensity of 150 $mW cm^{-2}$.

Table 1: Physicochemical properties of α-Fe_2O_3 nanoplates, nanocubes, and nanorods.

Sample	Length [nm]	Width [nm]	Height [nm]	SSA[a] [$m^2 g^{-1}$]	Dominant facets	Reaction rate constants k[b] [$\times 10^{-3}$ min^{-1}]	Normalized rate constants k_s[c] [$\times 10^{-4}$ $min^{-1} L m^{-2}$]
nanoplates	–	208.5 ± 27.3	14.6 ± 2.6	30.1 ± 4.1	{001}	4.38 ± 0.35	7.28 ± 1.14
nanocubes	22.0 ± 3.2	22.0 ± 3.2	22.0 ± 3.2	51.8 ± 8.0	{012}	28.20 ± 1.70	27.2 ± 4.5
nanorods	40.3 ± 8.7	10.9 ± 5.0	5.0 ± 1.2	119.8 ± 23.3	{001}{110}	73.26 ± 4.96	30.6 ± 6.3

[a] The specific surface area (SSA) and dominant facets are determined using TEM and AFM.[44,45] The density of hematite is 5.26 $g cm^{-3}$ from Cornell and Schwertmann.[46] [b] The apparent reaction rate constant (k) of RhB photodegradation on α-Fe_2O_3 architectures is calculated based on a pseudo-first-order kinetic model. [c] k_s denotes the rate constant (k) normalized to SSA, $k_s = k(\text{catalyst concentration} \times \text{SSA})^{-1}$.

a function of irradiation time. For comparison, an identical experiment in the dark was conducted in the presence of hematite and H_2O_2, and the data were shown in Figure S4 in the Supporting Information. Compared to that observed in the dark, the photocatalytic activity in the presence of light is dramatically enhanced. To evaluate the reactivity of hematite architectures quantitatively, the apparent reaction rate constant (k) of RhB degradation was calculated, and the results are summarized in Table 1 and the Supporting Information, Figure S5. For the blank experiment without catalysts, RhB degradation under visible-light illumination is relatively slow, with an apparent reaction rate constant $k = 1.65 \times 10^{-3}\,\mathrm{min}^{-1}$. With catalysts under the same experimental conditions, the reaction rate is dramatically promoted. To explore the intrinsic photoreactivity, k was normalized to the specific surface area (Table 1), referred to k_s.[44,48] Table 1 illustrates that at equivalent mass loadings, α-Fe_2O_3 nanorods exhibit the greatest photoreactivity with $k_s = 3.06 \times 10^{-3}\,\mathrm{min}^{-1}\,\mathrm{L\,m}^{-2}$, while k_s is 2.72×10^{-3} and $7.28 \times 10^{-4}\,\mathrm{min}^{-1}\,\mathrm{L\,m}^{-2}$ for nanocubes and nanoplates, respectively. The photonic efficiency ξ, which is defined as the ratio of the dye degradation rate and the incident photon flux at a given wavelength, is calculated according to Equation (1):[49]

$$\xi = \frac{hcN_A \Delta n_{\mathrm{RhB}}}{\Phi A \lambda} \qquad (1)$$

where h is Planck's constant, c is the velocity of light, N_A is Avogadro's constant, Δn_{RhB} is the difference of RhB concentration before and after photoreaction, Φ is light intensity, A is illuminated area, and λ is the wavelength of light. ξ at $\lambda = 420$ nm is 0.013 %, 0.0083 %, and 0.0072 % for nanorods, nanocubes, and nanoplates, respectively. The trend of ξ values essentially reflects that of the reaction rate constant k from above. Herein, ξ is estimated as the lower limit of photonic efficiency, taking into account the following factors:[50] First, the incident photons can be scattered by the suspended particles in an aqueous solution; second, the recombination rate of photogenerated electrons and holes is fast, and the annihilated charge carriers are not involved in relevant reaction processes. With regard to reaction products concerning RhB degradation, such as total organic carbon (TOC), intermediates, and inorganic mineralization species, detailed analyses are given in the Supporting Information (Tables S1, S2 and Figure S7–S9).

It is generally accepted that the reactivity of a photocatalyst is determined by its surface atomic and electronic structure.[10] The electronic structures of the as-prepared samples were investigated by diffuse-reflectance UV/Vis (DRUV/Vis) spectroscopy and high-resolution XPS. The absorption spectra converted to the Kubelka–Munk function (Supporting Information, Figure S6a) shows that all α-Fe_2O_3 samples share a comparable absorption edge around 550–600 nm. The band gap is determined to be 2.22, 2.23, 2.20 eV for nanoplates, nanocubes, and nanorods, respectively. The valence band spectra (Supporting Information, Figure S6b) illustrate that the line shape and the width of the band structure are almost identical. Regardless of the role of electronic structures in the heterogeneous photo-Fenton process, the as-prepared hematite architectures show comparable electronic structures, and the differences in the observed photocatalytic performance could be rationalized by the inherent variations in crystal facets exposed by α-Fe_2O_3 architectures.[24] Table 1 lists the dominant facets with large-percentage enclosed α-Fe_2O_3 architectures. The nanoplates mainly display the {001} facet, which presents either a single iron or single oxygen termination layer on the surface. For {001} facets with an iron termination layer, the density of low-coordinate surface iron cations is 4.6 atoms nm^{-2}. The above two coexisting but crystallographically distinct terminations of α-Fe_2O_3 {001} were observed under ultrahigh vacuum[51] and in aqueous solution.[52] Figure 3 a depicts the atomic model of {001} facet with an oxygen and iron termination layer, respectively. Given coexisting oxygen and iron of termination layers on the {001} facet, the fraction of surface low-coordinate iron cations on the {001} facet is further limited. On the other hand, both {012} (Figure 3 b) and {110} facets (Figure 3 c) display ridge-and-valley topography. This particular topography can expose a greater number of low-coordinate surface iron cations than the {001} facet with mixed oxygen and iron terminations. For example, the density of iron bonded to five oxygen anions (denoted as Fe_{5c}) on {110} and {012} is 10.1 and 7.3 atoms nm^{-2}, respectively. Unlike bulk iron cations, which are octahedrally coordinated by six oxygen anions, the coordinatively unsaturated iron cations can offer catalytically active sites for dye adsorbates, and the observed photoreactivity differences are a direct consequence of the availability of surface iron sites, with the reactivity following {110} > {012} ≫ {001}. The reaction mechanism for heterogeneous photo-Fenton catalysis involving photosensitization and catalytically active sites is discussed in detail in the Supporting Information. In contrast to previous studies focusing on amorphous and nonstoichiometric FeO_x catalysts in heterogeneous photo-Fenton catalysis,[28,29,54,55] our findings demonstrate that the construction of photocatalysts on the nanoscale with particular architectures and

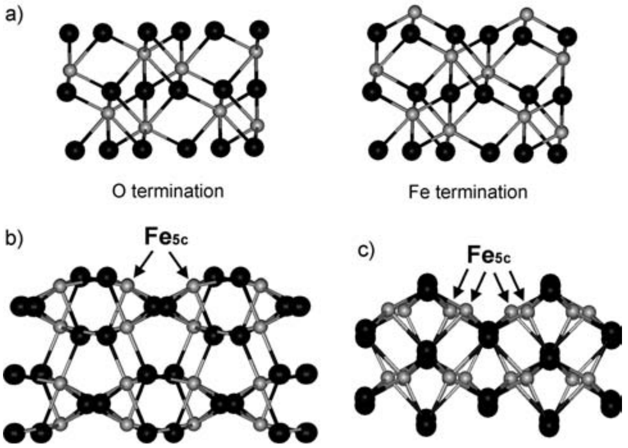

Figure 3. Side views of surface terminations of α-Fe_2O_3.[53] a) {001}, b) {012}, and c) {110}. Large black spheres are oxygen and small gray spheres are iron. The coordinatively unsaturated iron atoms on the {012} and {110} surfaces are shown by arrows.

associated facets is crucial when considering the design of high-performance nanocatalysts.

In conclusion, visible-light-induced RhB degradation with H_2O_2 at near neutral pH over hematite was strongly architecture-dependent and the reactivity trend can be rationalized as exposed facets in the order $\{110\} > \{012\} \gg \{001\}$. This study suggests a promising new strategy for engineering practical photocatalysts for wastewater treatment based on heterogeneous photo-Fenton oxidation. Furthermore, this study has broad implications in hematite-based water-splitting and solar cells, among others.

Experimental Section

All chemicals (ACS grade) were purchased from Alfa Aesar and used without further purification. Milli-Q water (18 MΩ cm in resistivity, Millipore Corporation) was used throughout the experiment.

The synthesis for hematite nanorods has been reported.[39,40,47] For the synthesis of rodlike goethite (α-FeOOH) precursors, dialyzed suspensions of ferrihydrite nanoparticles were quickly adjusted to pH 12 using a 5 M sodium hydroxide, and the resulting suspensions were aged at a specific temperature for 30–90 h. The aged suspensions were then dialyzed using a membrane (MWCO = 2000, SpectraPor) in Milli-Q water for three days. The dimensions of α-FeOOH nanorods can be tuned by changing the pH, aging temperature, and aging time. α-Fe_2O_3 nanorods were obtained by heating corresponding α-FeOOH precursors at 300 °C in air for 1 h. Nanocubes[41] and nanoplates[42] of hematite were synthesized following procedures reported previously and described in the Supporting Information.

Powder XRD data were collected using a Rigaku Corporation X-ray diffractometer (XRD-6000) with $Cu_{K\alpha}$ radiation ($\lambda =$ 0.154178 nm, 50 kV, 300 mA). Particle morphology was characterized on a Hitachi S4800 field-emission scanning electron microscope (SEM). TEM and HRTEM images were obtained using a Tecnai G^2 F20 U-TWIN microscope operating at 200 kV. Tapping-mode AFM measurements were carried out under ambient conditions using a Nanoscope IIIa (Veeco). Micro-Raman spectroscopy measurement was conducted using a Renishaw Micro-Raman Spectroscopy System (Renishaw in Via plus). A Renishaw red laser at 785 nm was employed as the excitation source. Diffuse-reflectance ultraviolet and visible (DRUV/Vis) spectra were obtained using a Perkin–Elmer Lambda 950 UV/Vis spectrometer. Fine $BaSO_4$ powder was used as a standard. X-ray photoelectron spectroscopy (XPS) data were obtained using an ESCALab 250 electron spectrometer from Thermo Scientific Corporation. Monochromatic 150 W $Al_{K\alpha}$ radiation was utilized and low-energy electrons were used for charge compensation to neutralize the samples. The binding energies were referenced to the adventitious C1s line at 284.8 eV. A Shirley-type background was subtracted from each spectrum and Avantage 4.15 software was used for curve-fitting. The atomic model of hematite facets was depicted using Materials Studio 5.5. Materials Studio is registered software of Accelrys Software Inc.

The photocatalytic activity of the as-prepared samples for the degradation of RhB in aqueous solutions was evaluated by measuring the absorbance of the irradiated solution. Prior to irradiation, 10 mg photocatalyst was mixed with RhB (50 mL, with a concentration of 0.02 mM) in a 100 mL round bottom flask. Afterwards, the suspension was magnetically stirred in the dark to reach a complete adsorption–desorption equilibrium, followed by the addition of 0.255 mL of hydrogen peroxide solution (H_2O_2, 30 wt %). The suspension (initial pH 6.8) was then illuminated by a 300 W xenon lamp. A cutoff filter of 420 nm was utilized to allow visible light to transmit, and a water filter was placed between the sample and the light source to eliminate infrared irradiation. The light intensity in the position of the center of the flask was measured to be about 150 mW cm^{-2} using a Newport optical power/energy meter (842-PE). During the irradiation, the reaction suspension was magnetically stirred and kept at RT. At certain time intervals, about 4 mL aliquots were sampled, centrifuged and filtered through a membrane (0.22 μm in diameter, Agela Technologies). The dye concentration in the filtrate was measured the absorption intensity of RhB at 554 nm using a PerkinElmer Lambda 950 UV/Vis spectrometer. The reaction products were evaluated using a series of analytical instruments described in the Supporting Information.

Received: July 18, 2011
Revised: September 19, 2011

Keywords: dyes/pigments · hematite · heterogeneous catalysis · photochemistry · photooxidation

---

[1] D. W. Goodman, *Chem. Rev.* **1995**, *95*, 523.
[2] G. A. Somorjai, *Chem. Rev.* **1996**, *96*, 1223.
[3] G. Ertl, *Angew. Chem.* **2008**, *120*, 3578; *Angew. Chem. Int. Ed.* **2008**, *47*, 3524.
[4] H.-J. Freund, G. Pacchioni, *Chem. Soc. Rev.* **2008**, *37*, 2224.
[5] J. T. Yates, C. T. Campbell, *Proc. Natl. Acad. Sci. USA* **2011**, *108*, 911.
[6] G. A. Somorjai, H. Frei, J. Y. Park, *J. Am. Chem. Soc.* **2009**, *131*, 16589.
[7] I. Lee, F. Delbecq, R. Morales, M. A. Albiter, F. Zaera, *Nat. Mater.* **2009**, *8*, 132.
[8] C. Burda, X. Chen, R. Narayanan, M. A. El-Sayed, *Chem. Rev.* **2005**, *105*, 1025.
[9] K. Rajeshwar, M. E. Osugi, W. Chanmanee, C. R. Chenthamarakshan, M. V. B. Zanoni, P. Kajitvichyanukul, R. Krishnan-Ayer, *J. Photochem. Photobiol. C* **2008**, *9*, 171.
[10] M. R. Hoffmann, S. T. Martin, W. Choi, D. W. Bahnemann, *Chem. Rev.* **1995**, *95*, 69.
[11] X. Chen, S. S. Mao, *Chem. Rev.* **2007**, *107*, 2891.
[12] H. Zhang, G. Chen, D. W. Bahnemann, *J. Mater. Chem.* **2009**, *19*, 5089.
[13] M. D. Hernández-Alonso, F. Fresno, S. Suárez, J. M. Coronado, *Energy Environ. Sci.* **2009**, *2*, 1231.
[14] I. Cesar, A. Kay, J. A. G. Martinez, M. Grätzel, *J. Am. Chem. Soc.* **2006**, *128*, 4582.
[15] H. Zhou, S. S. Wong, *ACS Nano* **2008**, *2*, 944.
[16] H. S. Kim, Y. Piao, S. H. Kang, T. Hyeon, Y. E. Sung, *Electrochem. Commun.* **2010**, *12*, 382.
[17] J. Park, K. J. An, Y. S. Hwang, J. G. Park, H. J. Noh, J. Y. Kim, J. H. Park, N. M. Hwang, T. Hyeon, *Nat. Mater.* **2004**, *3*, 891.
[18] S. Liu, J. Yu, M. Jaroniec, *J. Am. Chem. Soc.* **2010**, *132*, 11914.
[19] J. Li, D. S. Xu, *Chem. Commun.* **2010**, *46*, 2301.
[20] G. Liu, C. Sun, H. G. Yang, S. C. Smith, L. Wang, G. Q. Lu, H. M. Cheng, *Chem. Commun.* **2010**, *46*, 755.
[21] H. G. Yang, C. H. Sun, S. Z. Qiao, J. Zou, G. Liu, S. C. Smith, H. M. Cheng, G. Q. Lu, *Nature* **2008**, *453*, 638.
[22] A. Selloni, *Nat. Mater.* **2008**, *7*, 613.
[23] H. G. Yang, G. Liu, S. Z. Qiao, C. H. Sun, Y. G. Jin, S. C. Smith, J. Zou, H. M. Cheng, G. Q. Lu, *J. Am. Chem. Soc.* **2009**, *131*, 4078.
[24] J. Pan, G. Liu, G. Q. Lu, H. M. Cheng, *Angew. Chem.* **2011**, *123*, 2181; *Angew. Chem. Int. Ed.* **2011**, *50*, 2133.
[25] C. Z. Wen, H. B. Jiang, S. Z. Qiao, H. G. Yang, G. Q. Lu, *J. Mater. Chem.* **2011**, *21*, 7052.
[26] C. Z. Wen, J. Z. Zhou, H. B. Jiang, Q. H. Hu, S. Z. Qiao, H. G. Yang, *Chem. Commun.* **2011**, *47*, 4400.
[27] C. Z. Wen, Q. H. Hu, Y. N. Guo, X. Q. Gong, S. Z. Qiao, H. G. Yang, *Chem. Commun.* **2011**, *47*, 6138.

[28] M. Hartmann, S. Kullmann, H. Keller, *J. Mater. Chem.* **2010**, *20*, 9002.

[29] J. Herney-Ramirez, M. A. Vicente, L. M. Madeira, *Appl. Catal. B* **2010**, *98*, 10.

[30] Y. Yin, A. P. Alivisatos, *Nature* **2005**, *437*, 664.

[31] Y.-W. Jun, J.-S. Choi, J. Cheon, *Angew. Chem.* **2006**, *118*, 3492; *Angew. Chem. Int. Ed.* **2006**, *45*, 3414.

[32] N. Tian, Z.-Y. Zhou, S.-G. Sun, Y. Ding, Z. L. Wang, *Science* **2007**, *316*, 732.

[33] A. R. Tao, S. Habas, P. D. Yang, *Small* **2008**, *4*, 310.

[34] Y. Xia, Y. Xiong, B. Lim, S. E. Skrabalak, *Angew. Chem.* **2009**, *121*, 62; *Angew. Chem. Int. Ed.* **2009**, *48*, 60.

[35] H. C. Zeng, *J. Mater. Chem.* **2006**, *16*, 649.

[36] H. C. Zeng, *Int. J. Nanotechnol.* **2007**, *4*, 329.

[37] L. Vayssieres, C. Sathe, S. M. Butorin, D. K. Shuh, J. Nordgren, J. Guo, *Adv. Mater.* **2007**, *17*, 2320.

[38] S. K. Mohapatra, S. E. John, S. Banerjee, M. Misra, *Chem. Mater.* **2009**, *21*, 3048.

[39] X. B. Mao, H. C. Yang, X. M. Zhou, C. X. Wang, Y. S. Wang, Y. L. Yang, C. Wang, G. Liu, *Cryst. Growth Des.* **2010**, *10*, 504.

[40] H. C. Yang, X. B. Mao, Y. J. Guo, D. W. Wang, G. Ge, R. Yang, X. Qiu, Y. L. Yang, C. Wang, Y. S. Wang, G. Liu, *CrystEngComm* **2010**, *12*, 1842.

[41] X. Liang, X. Wang, J. Zhuang, Y. Chen, D. Wang, Y. Li, *Adv. Funct. Mater.* **2006**, *16*, 1805.

[42] L. Chen, X. Yang, J. Chen, J. Liu, H. Wu, H. Zhan, C. Liang, M. Wu, *Inorg. Chem.* **2010**, *49*, 8411.

[43] G.-S. Park, D. Shindo, Y. Waseda, T. Sugimoto, *J. Colloid Interface Sci.* **1996**, *177*, 198.

[44] J. J. Erbs, B. Gilbert, R. L. Penn, *J. Phys. Chem. C* **2008**, *112*, 12127.

[45] R. L. Penn, personal communications.

[46] R. M. Cornell, U. Schwertmann, *The Iron Oxides: Structure, Properties, Reactions, Occurrences, and Uses*, 2nd ed., Wiley-VCH, Weinheim, **2003**.

[47] X. M. Zhou, H. C. Yang, C. X. Wang, X. B. Mao, Y. S. Wang, Y. L. Yang, G. Liu, *J. Phys. Chem. C* **2010**, *114*, 17051.

[48] A. J. Anschutz, R. L. Penn, *Geochem. Trans.* **2005**, *6*, 60.

[49] I. Bannat, K. Wessels, T. Oekermann, J. Rathousky, D. Bahnemann, M. Wark, *Chem. Mater.* **2009**, *21*, 1645.

[50] K. Chiang, R. Amal, T. Tran, *J. Mol. Catal. A* **2003**, *193*, 285.

[51] X. G. Wang, W. Weiss, S. K. Shaikhutdinov, M. Ritter, M. Petersen, F. Wagner, R. Schlögl, M. Scheffler, *Phys. Rev. Lett.* **1998**, *81*, 1038.

[52] C. M. Eggleston, A. G. Stack, K. M. Rosso, S. R. Higgins, A. M. Bice, S. W. Boese, R. D. Pribyl, J. J. Nichols, *Geochim. Cosmochim. Acta* **2003**, *67*, 985.

[53] J. G. Catalano, P. Fenter, C. Park, Z. Zhang, K. M. Rosso, *Geochim. Cosmochim. Acta* **2010**, *74*, 1498.

[54] M. Cheng, W. Song, W. Ma, C. Chen, J. Zhao, J. Lin, H. Zhu, *Appl. Catal. B* **2008**, *77*, 355.

[55] W. Du, Q. Sun, X. Lv, Y. M. Xu, *Catal. Commun.* **2009**, *10*, 1854.